Fluid-induced microseismicity in pre-stressed rock masses

M. Schoenball,[1]* T. M. Müller,[2] B. I. R. Müller[1] and O. Heidbach[1]†

[1]*Geophysical Institute, Karlsruhe Institute of Technology, Hertzstr. 16, 76187 Karlsruhe, Germany. E-mail: martin.schoenball@kit.edu*
[2]*CSIRO Petroleum, Australian Ressources Research Centre, Kensington WA 6151, Australia*

SUMMARY

We model microseismicity triggered by fluid injection on the basis of the theory of poroelasticity accounting for the external stress field. Consideration of the fully coupled poroelastic field equations enables us to apply a Coulomb failure criterion using pore fluid pressure and stress tensor as well as the coefficient of friction. The poroelastic fields are calculated with the finite-element method simulating fluid injection with constant injection rate into a 2-D domain. The influence of diffusivity, injection rate and stress field on the occurrence of microseismicity is analysed and compared to simulations based on pore fluid pressure diffusion only. We show that an anisotropic initial stress field causes elongated microseismic clouds. These clouds are indistinguishable from those generated in poroelastic solids under isotropic stress but exhibiting anisotropic hydraulic diffusivity. This similarity shows that microseismicity distributions dependent on both, the hydraulic properties and the coupling of pore fluid pressure to the stress field. In particular, neglecting the influence of the external stress field may lead to overestimation of the anisotropy of diffusivity tensor components. Furthermore, the results of our numerical simulations are strongly sensitive to changes of fluid injection rate.

Key words: Geomechanics; Permeability and porosity; Plasticity; diffusion; and creep; Fracture and flow; Fractures and faults; Mechanics; theory; and modelling.

GJI Seismology

1 INTRODUCTION

The occurrence of microseismicity is a phenomenon often observed during or after fluid injection in a well bore. Injection experiments are performed by the oil industry to increase the hydraulic connectivity between the well bore and reservoir formation (Fokker 2006), in geothermal reservoir exploration for fluid flow stimulation (Dyer *et al.* 1994), and in scientific boreholes such as the KTB borehole to investigate the state of stress (Zoback & Harjes 1997). Fig. 1 shows a map view of the recorded and localized microseismic events of the 1993 injection experiment at the GPK2 bore hole in Soultz (Dyer *et al.* 1994) and the event sequence in a distance-to-injection-point versus time-of-occurrence plot (in the following called *r–t* plot). Fig. 1(a) indicates that the microseismic events are distributed preferentially along an orientation which approximately coincides with the orientation of maximum horizontal stress, that is about N170° (Cornet *et al.* 2007). This alignment produces an elliptical shape of the microseismicity cloud interpreted as fracture opening along this direction (Baria *et al.* 1995).

*Now at: Institute of Soil Mechanics and Rock Mechanics, Karlsruhe Institute of Technology, 76128 Karlsruhe, Germany.
†Now at: Helmholtz Centre Potsdam, GFZ German Research Centre for Geosciences, Telegrafenberg 326, 14473 Potsdam, Germany.
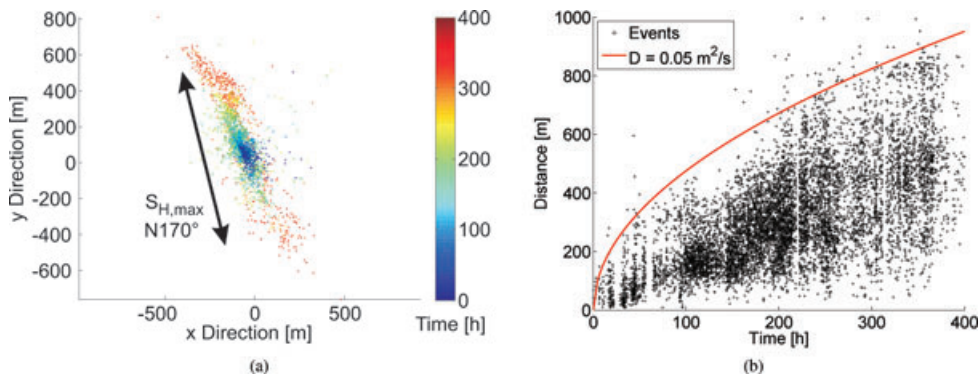
The interpretation and modelling of induced microseismicity has attracted considerable interest as it may reveal information about subsurface fluid transport properties (e.g. Talwani *et al.* 2007). According to the current understanding microseismicity results from a decrease in effective normal stresses on fractures optimally oriented for reactivation as a consequence of elevated pore fluid pressure (Fehler 1989).

Shapiro *et al.* (1999) assume that the elliptical shape of the microseismic cloud is a result of anisotropic diffusivity. They hypothesise that a pore fluid pressure perturbation caused by a point injection behaves like a low-frequency second-type compressional Biot wave and can therefore be described by the equation of diffusion (Biot 1962). Further assuming that the Earth's crust is in a subcritical stress state such that even small changes of pore fluid pressure may induce rock failure Shapiro *et al.* (1999) retrieve the relation in time and space for the first events triggered by injection of fluid with constant pressure at the source point:

$$r = \sqrt{4\pi Dt}, \tag{1}$$

where r is distance from injection source, D is the fluid pressure diffusivity and t is time from beginning of injection. This approach, the so-called seismicity based reservoir characterization (SBRC), was applied to the hot dry rock (HDR) test sites of Fenton Hill and Soultz-sous-Forêts (Shapiro *et al.* 2002) to obtain field-scale

Figure 1. (a) Microseismicity cloud observed during the 1993 injection test in GPK2 bore hole (Dyer 1994) with orientation of maximum horizontal stress, $S_{H,max}$. The colours denote the occurrence time after beginning of injection. (b) *r–t* plot with field-scale estimate of diffusivity after Shapiro *et al.* (1999).

estimates of the diffusivity and diffusivity tensors (see also the parabola in Fig. 1b).

A modelling approach based on the SBRC assumptions was developed by Rothert (2004). First, the migration of a pore fluid pressure perturbation induced by the injection is modelled by solving the partial differential equation of pressure diffusion. Second, a so-called random criticality field of rock strength is created that represents the critically stressed crust. Third, a microseismic event is then triggered when the local fluid pressure exceeds the criticality (rock strength) value, that is, the condition for failure is reached. Using this modelling approach Rothert (2004) was able to reproduce the spatio-temporal evolution of observed microseismic events. In Hummel & Müller (2009) this approach was extended to non-linear pore fluid pressure diffusion.

Bruel (2007) investigates the SBRC approach by means of a geomechanical model. Following the SBRC assumptions he implements an *a priori* anisotropic diffusivity using a large set of preferentially aligned fractures. The randomness of the criticality field of rock strength in the approach of Rothert (2004) is replaced by a given configuration of fractures. In this fracture network fluid flow is calculated according to an analytical solution for fluid flow between parallel surfaces. The opening of fractures due to fluid flow induces stress changes in the purely elastically assumed volume. As a result Bruel (2007) obtains microseismicity distributions similar to those of Rothert (2004) and the observed ones (Baria *et al.* 1995). A similar numerical procedure has been suggested by Guglielmi *et al.* (2008) and was applied to a known distribution of fracture planes.

In the aforementioned works the shapes of induced microseismicity 'clouds' are exclusively attributed to the tensorial character of the diffusivity, that is, to an intrinsic property of the fluid-saturated rock. According to this interpretation the probability for triggering microseismic events at larger distances from the injection point increases for directions with higher pressure diffusivity as the induced pressure perturbation migrates faster (Baria *et al.* 1995). This point of view is conform with the interpretation that flow diffusivity is largest in the fracture plane and therefore an aligned set of fractures results in an effective anisotropic diffusivity (Barton 2007).

However, these approaches do not consider the feedback process between fluid flow through the porous rock volume and its interaction with the stress tensor. This would require the solution of the poroelastic field equations. One intrinsic characteristic of poroelasticity is the coupling between pore fluid pressure and the stress field. The effect of the so-called pore fluid pressure–stress coupling has a significant impact on rock failure (e.g. Hillis 2000). Through 'pore fluid pressure–stress coupling' the principle stresses are changed

differently, thus leading to a change of the Mohr circles radius, whereas according to Terzaghis principle of effective stresses the pore fluid pressure affects the principle stresses equally. At a given location this coupling effect might change the criticality of a stress state crucially. Furthermore, the coupling becomes important when describing the stress state and its spatio-temporal evolution in compacting reservoirs during depletion (Rudnicki 1986; Engelder & Fischer 1994; Hillis 2000).

In this paper, we investigate systematically to what extent the external (present-day tectonic) stress field controls a spatial microseismicity distribution. For this purpose we follow a new modelling concept that uses the quasi-static poroelastic field equations. Rock failure, and hence the creation of a microseismic event, is modelled using the Coulomb failure criterion. By solving the poroelastic field equations with a constant-injection-rate source term we compute stresses and pore fluid pressure and 'create' a microseismic event provided that the Coulomb failure criterion in an fictitious failure plane is satisfied. We do not aim at explaining any particular observation but to investigate the principal influence of poroelastic interaction on the spatio-temporal evolution of microseismicity. We discuss the sensitivity of microseismic clouds to constant-injection-rate sources compared to constant-pressure sources. Our results show that the elongated shape of microseismic clouds can also be explained by anisotropic *in situ* stress distributions and that the injection rate has a significant influence on the spatio-temporal evolution of microseismicity.

2 MODEL CONCEPT

Our aim is to investigate the link between pore fluid pressure–stress coupling and microseismicity. Therefore, our model setup and model parameters are chosen to represent a general setting rather than rock properties from specific sites. The following sections describe the geometrical setup, the parameters chosen and the equations, which are solved in the numerical modelling.

2.1 Setup of numerical experiments

We perform our 2-D numerical experiment simulating fluid injection from a source into a rock volume with homogeneous rock properties (Table 1). The model of the poroelastic solid consists of a circular region of 1000 m radius with the injection source in the centre (Fig. 2).

A point injection is simulated by a source region of 5 mm diameter. According to the Kirsch equations (Jaeger *et al.* 2007) the

Table 1. Material properties of the modelled rock.

Material properties	
Bulk modulus of solid grains, K_g	40 GPa
Bulk modulus of fluid, K_f	2 GPa
Poisson's ratio, ν	0.25
Elastic tensile limit, p_t^{el}	150 MPa
Drained bulk modulus, K_d	30 GPa
Porosity, ϕ	0.2
Fluid density, ρ_0	1000 kg m^{-3}

Table 2. Summary of the parameters used in the numerical experiments.

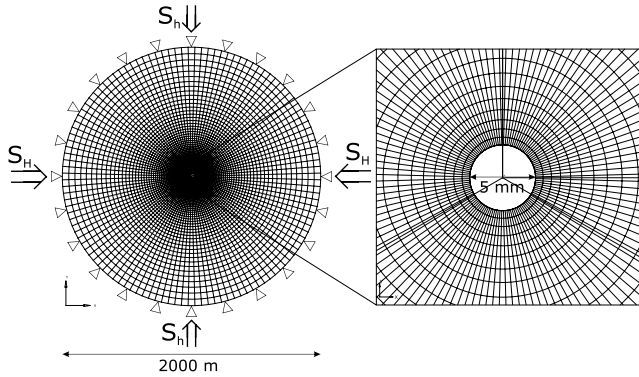| Exp.	Diffusivity (m^{2}s^{-1})	Stress field (MPa)	Inj. rate (l s^{-1}m^{-1})
1	$D_{xx} = 0.01, D_{yy} = 0.01$	$\sigma_{xx} = 1, \sigma_{yy} = 1$	$q = 0.15$
2	$D_{xx} = 0.02, D_{yy} = 0.02$	$\sigma_{xx} = 1, \sigma_{yy} = 1$	$q = 0.15$
3	$D_{xx} = 0.01, D_{yy} = 0.01$	$\sigma_{xx} = 1, \sigma_{yy} = 1$	$q = 0.075$
4	$D_{xx} = 0.02, D_{yy} = 0.01$	$\sigma_{xx} = 1, \sigma_{yy} = 1$	$q = 0.15$
5	$D_{xx} = 0.01, D_{yy} = 0.01$	$\sigma_{xx} = 1, \sigma_{yy} = 0.6$	$q = 0.15$

Figure 2. Mesh of the model. The model consists of 17 280 plane strain elements. Each element is a 3° section of a ring around the injection source, thus the element size increases with increasing distance from the injection yielding a high resolution at the centre where high pore fluid pressure gradients are expected.

influence by such a small hole on the stress field decays within few tens of millimetres. This influence can be neglected as we investigate microseismicity on the metre scale. The 3-D representation of this source geometry is an infinite line source, which is a good first approximation of a well bore with an open section of several metres. Boundary conditions of the model are: (1) A fluid injection with a constant injection rate, (2) the displacements at the boundary are zero and (3) no fluid can flow out of the model, that is, undrained boundary conditions are applied. In order to prevent any influence on the poroelastic fields caused by the finite size of the modelling domain and the undrained boundary condition, only the innermost region with radius of 100 m is used for subsequent data analysis. In order to investigate the influence of the external stress field we add initial stress conditions to the stress field. We solve the coupled differential equations numerically with the finite element method using the commercial software package Abaqus^{TM}, version 6.6-1 (Dassault Systèmes Simulia Corp.). The solution scheme implemented in Abaqus has been validated by Altmann *et al.* (2008) against the analytical solution for a point injection in a 3-D space by Rudnicki (1986). In general, Abaqus is capable of simulating non-linear poroelasticity where the drained bulk modulus K_d is dependent on the pore fluid pressure. This non-linear behaviour can be controlled via the elastic tensile limit e_t^{el}. In our approach, we did not want to study the influence of a variable bulk modulus and thus have chosen the bulk modulus to be constant. This is achieved under the assumption of a large value for the elastic tensile limit. This approach is justified since our stress conditions are non-tensile stress conditions for which the actual tensile strength of the rock is not to be considered when assessing rock failure.

We performed five numerical experiments with different initial stress conditions (isotropic and anisotropic), diffusivity (isotropic and anisotropic) and injection rates, as summarized in Table 2.

Here isotropic and anisotropic stress conditions denote initial stress conditions with equal and unequal principal stresses, respectively.

2.2 Equations of quasi-static poroelasticity

The poroelastic field equations solved in our numerical experiments are represented by the Beltrami–Michell equations (Wang 2000, eq. 4.27)

$$\nabla^2 \sigma_{ij} + \frac{1}{1+\nu}\frac{\partial^2 \sigma_{kk}}{\partial x_i \partial x_j} + \frac{1-2\nu}{1-\nu}\alpha\left(\frac{1-\nu}{1+\nu}\frac{\partial^2 p}{\partial x_i \partial x_j} + \delta_{ij}\nabla^2 p\right)$$
$$= -\frac{1}{1+\nu}\delta_{ij}\nabla\mathbf{F} - \frac{\partial F_i}{\partial x_j} - \frac{\partial F_j}{\partial x_i} \tag{2}$$

and a pore fluid pressure–mean stress equation including the fluid source Q, the injected volume of fluid per bulk volume per time (Wang 2000, eq. 4.63):

$$\frac{\alpha}{K_d B}\left(\frac{B}{3}\frac{\partial \sigma_{kk}}{\partial t} + \frac{\partial p}{\partial t}\right) - \frac{k}{\eta}\nabla^2 p = Q. \tag{3}$$

Here σ_{ij} are the total stress tensor components and σ_{kk} is the total mean stress, x_i and x_j are the coordinates. The body force $\mathbf{F}$ usually is gravity and can be neglected in our scenario. ν is Poisson's ratio, p is pore fluid pressure, α is the Biot–Willis coefficient, K_d is the drained bulk modulus of the rock mass, δ_{ij} is the Kronecker symbol, B is Skempton's coefficient (Wang 2000), k is fluid permeability and η is the fluid viscosity. The relation between permeability k and diffusivity D is given by $D = Nk/\eta$, where N is a poroelastic modulus (Dutta & Odé 1979). The poroelastic field eqs (2) and (3) enable us to model the coupled process of pore fluid pressure and stress diffusion in a deformable porous solid. This set of partial differential equations is a natural extension of the pressure diffusion equation when the coupling to stresses in the rock matrix is accounted for.

2.3 Analysis of microseismicity

Whereas the equation of diffusion only describes the pore fluid pressure, eqs (2) and (3) yield the pore fluid pressure and the full stress tensor. These quantities enables us to apply the Coulomb failure criterion on deciding whether an event is triggered or not. We replace the random criticality field used in the SBRC approach (Rothert & Shapiro 2007) by a failure envelope characterized by the rock parameters, coefficient of friction and cohesion (*cf.* Fig. 3). Bruel (2007) also used a Coulomb failure criterion to generate microseismicity. However he neglected poroelastic effects for the calculation of the stress state.

By solving eqs (2) and (3) we retrieve the pore fluid pressure and the stress tensor components from which we calculate the effective stresses

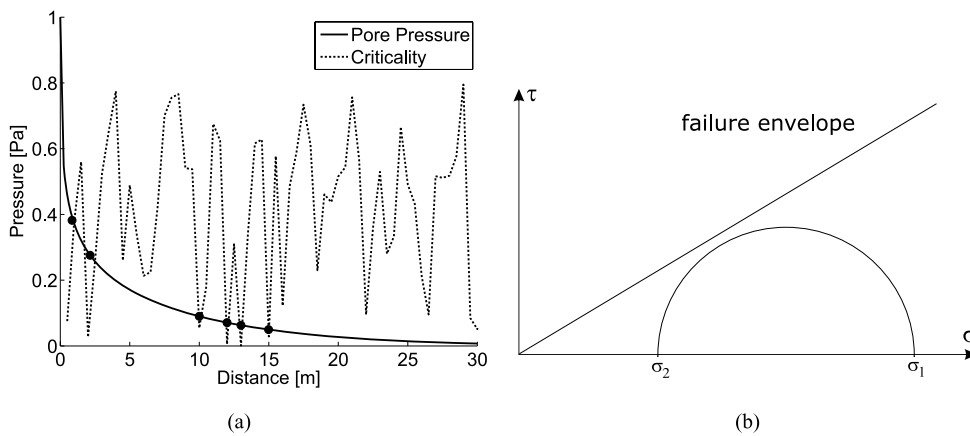$$\sigma_{i,\text{eff}} = \sigma_i - p. \tag{4}$$

Figure 3. (a) Profile of calculated pore fluid pressure for an injection source at the origin with fixed pore fluid pressure of 1 Pa and a diffusivity of the material of $1\,\mathrm{m^2\,s^{-1}}$ and randomly chosen criticality through a 2-D model domain. Dots represent locations where an event is triggered. (b) The Coulomb failure criterion used in our approach. The principal stresses are connected by the Mohr circle, if it touches the failure envelope an event is triggered.

The Coulomb failure criterion is used to generate microseismic events from these effective stresses. In order to do so the effective principal stresses are used to calculate maximum shear stresses $\tau_{\max} = \frac{1}{2}(\sigma_{1,\mathrm{eff}} - \sigma_{2,\mathrm{eff}})$ and mean stresses $\sigma_{\mathrm{mean}} = \frac{1}{2}(\sigma_{1,\mathrm{eff}} + \sigma_{2,\mathrm{eff}})$. Maximum shear and mean stresses are used in the failure criterion (Jaeger *et al.* 2007)

$$\tau_{\max} \geq S_0 \cos\varphi + \sigma_{\mathrm{mean}} \sin\varphi. \tag{5}$$

S_0 is cohesion and φ is the friction angle, which is related to the friction coefficient μ by $\tan\varphi = \mu$. Using eq. (5) we assume optimally oriented failure planes at every point, which are most likely to rupture. While this will not produce randomly distributed events as observed, it delivers the information contained in the triggering front of the first possible events. The rupture process has no influence on the transport properties, that is, fractures are not opened and diffusivity is not increased due to rupture. Furthermore, every failure plane is only allowed to rupture once. These conditions imply the assumption that microseismicity is a 'passive tracker' of fluid pressure rather than a process that affects fluid pressure propagation.

3 POROELASTIC EFFECTS ON MICROSEISMICITY

In the following section, five numerical experiments are described and discussed. The first numerical experiment conducted with isotropic diffusivity and initial stress field serves as reference for further numerical experiments. In the second and third numerical experiment we changed the magnitude of diffusivity and injection rate, respectively. The fourth experiment investigates the influence of anisotropic diffusivity and the fifth experiment that of an anisotropic initial stress field. In all experiments cohesion was set to zero in the Coulomb criterion. The parameters used for each numerical experiment are summarized in Table 2 and are also printed on the plots.

All *r–t* plots generated with our model have a parabolic triggering front similar to the results of Shapiro *et al.* (1999) but now derived by a failure criterion approach applied to a poroelastic medium.

3.1 Isotropic initial stress field and diffusivity

Applying an isotropic stress state and isotropic diffusivity results in an isotropic seismicity cloud (Fig. 4a). Due to our deterministic

failure criterion we obtain a sharp triggering front. Note that the discrete spatio-temporal evolution of the failure curves originates in the discrete time steps of the numerical solution. After each step failure is reached for a certain range of radii.

The influence of the coefficient of friction on the triggering front can be studied from the *r–t* plot where the triggering fronts for $\mu = 0.4, 0.6$ and 0.8 are shown. For the case of lower friction the triggering front propagates faster compared to the case with a higher coefficient of friction, that is, the rock is less stable and thus more likely to rupture.

3.2 Influence of diffusivity and injection rate

The second and third experiments were performed to study the influence of the magnitudes of diffusivity and injection rate (Figs 4b and c). These two numerical experiments show that there is almost no response to a change in diffusivity, but that the microseismic event distribution is very sensitive to a change in injection rate. In the SBRC approach the migration velocity of the pore fluid pressure perturbation and the triggering front is proportional to the square root of diffusivity. The poroelastic results differ from that of the SBRC approach: the migration velocity of the triggering front shows only a slight increase with increasing diffusivity. The reasons are twofold, first a higher diffusivity corresponds to a faster propagation of the pore fluid pressure perturbation. But this is counteracted by the constant injection rate. In our approach the pore fluid pressure perturbation is calculated from the input parameters, one is the injection rate q which corresponds to the work applied at the source and is kept constant. To reach failure at a given location a sufficient pore fluid pressure build-up is necessary. In a rock with a high diffusivity a lower pore fluid pressure will develop compared to a rock with low diffusivity when the same rate of fluid injection is applied. Thus, it will take longer to reach the pore fluid pressure threshold to generate events. The SBRC approach on the other hand does not consider the injection rate but it is always assumed large enough to maintain the pore fluid pressure perturbation constant at the injection point independent of diffusivity. Thus work applied to the source must increase with increased diffusivity.

The fourth experiment was performed to study the effect of an anisotropic diffusivity. This results in an elongated shape of the synthetic seismicity cloud in direction of the larger diffusivity (Fig. 4d), which is in agreement with the SBRC approach. The broadened *r–t*
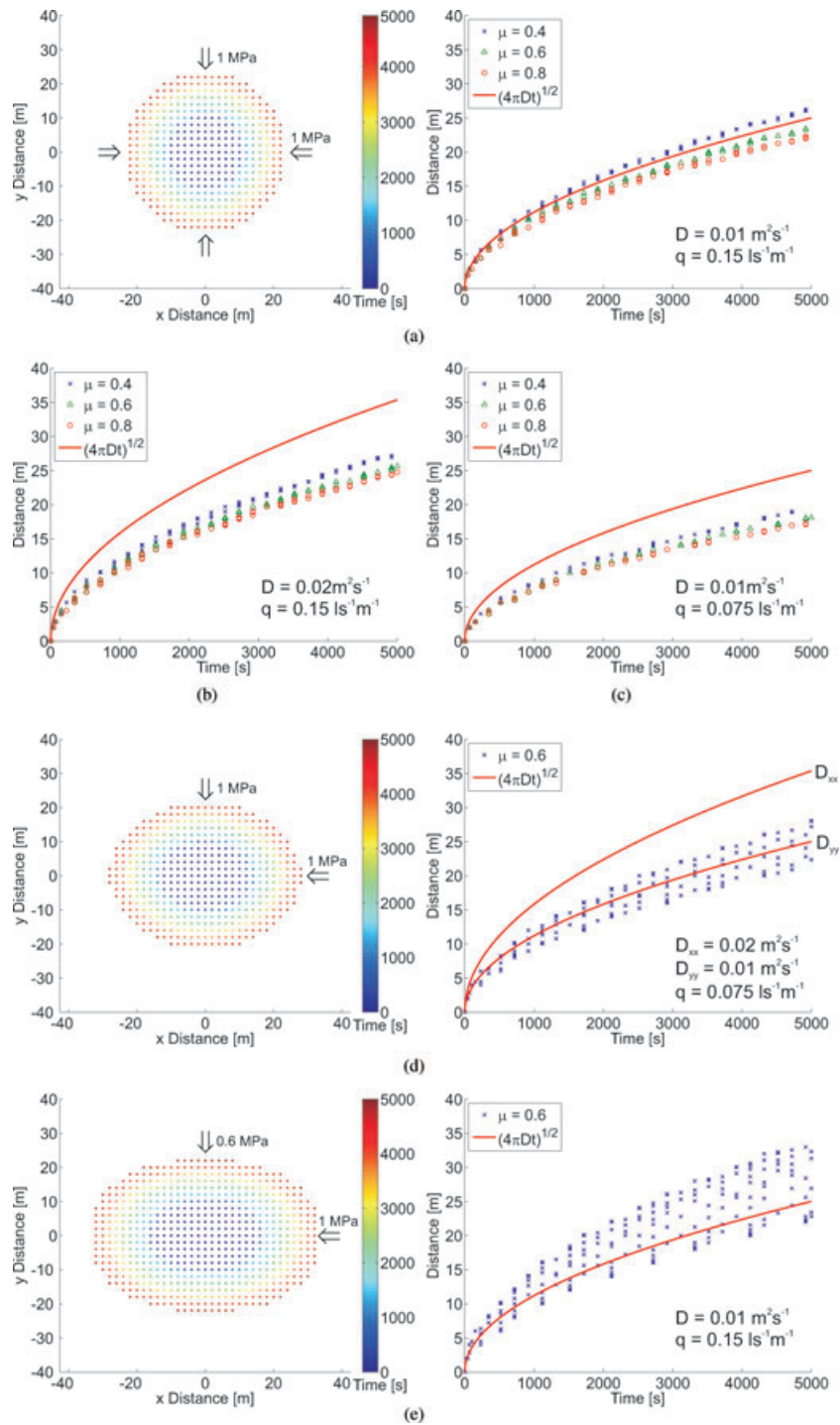
Figure 4. Synthetic microseismic clouds and *r*–*t* plots for the numerical experiments 1–5 (Table 2). The cloud plots are for a coefficient of friction of $\mu = 0.6$, the occurrence times of the synthetic microseismic events are colour coded. The *r*–*t* plots for experiments are for three different coefficents of frictions: crosses $\mu = 0.4$, triangles $\mu = 0.6$ and circles $\mu = 0.8$. The red curves denote the triggering front according to eq. (1).

plot is caused by simultaneous failures at different azimuths and thus at different radii from the injection source.

3.3 Anisotropic initial stress field

In the fifth experiment we study the effect of an anisotropic initial stress field (Fig. 4e). This results in an elongated seismicity cloud, strongly resembling that for anisotropic diffusivity but isotropic

initial stresses depicted in Fig. 4(d). Applied to experiments and real data it will be impossible to distinguish between these two kinds of anisotropy alone from the microseismic data.

The stress state can be described by means of Mohr circles. Prior to injection the Mohr circles are identical throughout the model because the external stresses are the same at every point of the model. To obtain the effective stresses we subtract the pore fluid pressure from the normal components of the total stress tensor. According
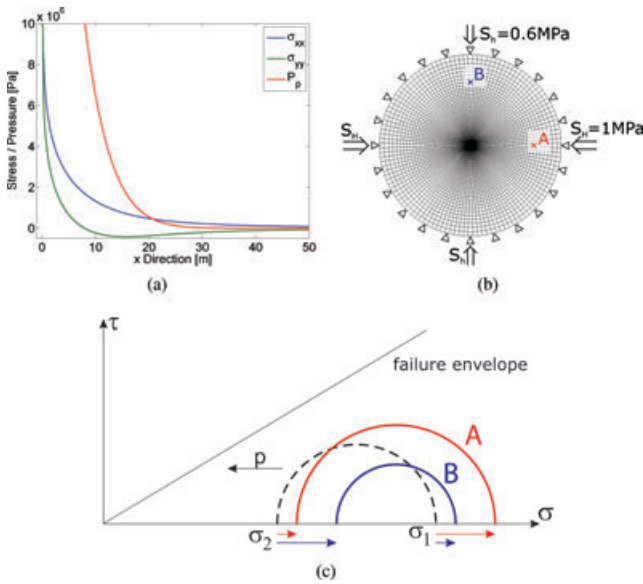
Figure 5. (a) Plot of principal stresses and pore fluid pressure according to eqs (6) and (7) along the x-direction. Note that σ_{xx} is always larger than σ_{yy}. (b) Location of the points A and B in an anisotropic stress field with the orientation of the maximum horizontal stress $S_{H,\max}$ along the x-direction. (c) Mohr circles for points A and B in (b) with total stresses. The dashed circle represents the stress state prior to injection. The red circle represents the stress state at point A after injection, the blue that at point B. To obtain the effective stresses both circles must be shifted to the left-hand side by the same amount of pore fluid pressure p.

to the traditional effective stress principle the total stresses do not change with pore fluid pressure. Therefore, after injection, the pore fluid pressure distribution is radially symmetric and thus, the position of the Mohr circle along the axis of effective normal stress is varying according to the radial distance of the considered location with respect to the injection point, but not as a function of the azimuthal position. This approach would fail to explain modelled asymmetry of the microseismicity cloud.

If we consider poroelasticity the total stresses ($\sigma_{i,\text{tot}} = \sigma_{i,\text{eff}} + p$) are not only changed by pore fluid pressure but due to pore fluid pressure–stress coupling also by a magnitude of additional stress induced by the injection as derived by Rudnicki (1986)

$$p = \frac{q\eta}{4\pi k\rho_0} E_1\left(\frac{R^2}{4Dt}\right) \qquad (6)$$

$$\sigma_{ij} = \frac{q\alpha\eta G}{4\pi\rho_0 k\left(K_d + \frac{4}{3}G\right)}$$
$$\cdot \left\{\left(\delta_{ij} - \frac{2x_i x_j}{R^2}\right)\frac{4Dt}{R^2}\left[1 - e^{-\frac{R^2}{4Dt}}\right] - \delta_{ij}E_1\left(\frac{R^2}{4Dt}\right)\right\} \qquad (7)$$

with the exponential integral

$$E_1 = \int_z^\infty \frac{e^{-s}}{s}\,\mathrm{d}s. \qquad (8)$$

Here we have the injection rate q in fluid mass per time and per unit length, mass density of the fluid ρ_0, the shear modulus G, the distance from injection point R and the coordinates of the point of observation x_i and x_j. According to eqs (6) and (7), the stress change along the radial direction is larger than that in tangential direction

with respect to the injection point, the stress change in tangential direction may even be negative (Fig. 5a).

If we assume anisotropic far-field tectonic stresses to $S_{H,\max}$ in x-direction and superimpose this field with the Rudnicki stress field for an injection we see the following phenomena: at point A in Fig. 5(b) the contribution of the now radially oriented σ_{xx} to $S_{H,\max}$ is larger than that of σ_{yy}, which is in tangential direction, to $S_{h,\min}$ (eq. 7)—the Mohr circle becomes larger (Fig. 5c) and little shifted to the right-hand side. If we look at point B, the effect will be vice versa. Now σ_{yy} is oriented radially and thus larger than σ_{xx}. $S_{H,\max}$ is increased by a smaller magnitude than $S_{h,\min}$ and the Mohr circle gets smaller and more shifted to the right-hand side—thus it represents a more stable condition and will break later compared to point A. Along the y-axis the rock is more stable than along the x-axis which leads to an elongated microseismicity cloud.

4 DISCUSSION

Our synthetic microseismicity clouds show two principal deviations compared to the ones by Rothert (2004). First, our triggering front does not coincide with that expected from the SBRC approach (Fig. 4). In the SBRC approach the only parameters that control the triggering front are diffusivity and the *a priori* given criticality field. In contrast, in our numerical model setup the spatio-temporal evolution of the triggering front is dependent on the applied stress state, injection rate, diffusivity and the coefficient of friction. This principal disparity in obtaining synthetic microseismic clouds results in different triggering fronts. However, these differences have no impact on our general findings that anisotropic stress contributes to the spatio-temporal evolution of the triggering front.

In contrast to observed microseismic clouds and also those generated by Rothert (2004), our numerical model does not produce events behind the triggering front because we only consider one rupture event per gridpoint and do not consider the processes of local stress build-up after a first rupture event which may lead to subsequent events. A second reason is that we did not include any randomness in our model. This may be done at the point of the failure criterion in giving every gridpoint a different cohesion and/or different coefficient of friction. However, the lack of events behind the triggering front has no influence on the actual triggering front that is used to derive the hydraulic *in situ* properties of a reservoir.

The neglect of a dynamically increased diffusivity after rupture and the assumption of optimally oriented failure planes is a rough oversimplification but yields reasonable results for the triggering front which is used by the SBRC method to characterize diffusivity and represented by only the first triggered events in an otherwise undisturbed rock.

An important observation from our results is the influence of the fluid injection rate on the triggering front. This sensitivity to injection rate is related to the implementation of the fluid source. In this work, it is realized as a constant-injection-rate source, whereas Rothert (2004) implements the fluid source as a constant-pressure source. Our results indicate that the implementation of the fluid source may be a critical issue and needs further investigations. Our implementation probably overestimates the effect of the injection rate on the pressure on the bore hole wall since Baisch & Harjes (2003) observed that an increase of injection rate may result only in a slight increase of injection pressure. From similar observations Hillis (2000) concludes that rock failure acts as a valve limiting the maximum pore fluid pressure that can develop. Nevertheless, assuming that the injection rate increases the injection pressure it
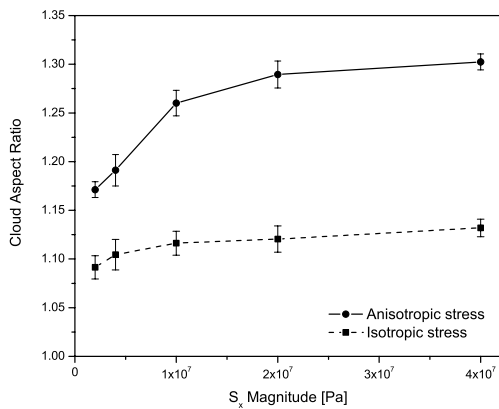
Figure 6. Aspect ratio of synthetic microseismic clouds over magnitude of initial stresses for an anisotropic stress field with constant $S_{h,min}/S_{H,max}$ ratio of 0.8 and isotropic diffusivity and for an isotropic stress field with anisotropic diffusivity with D_{xx}/D_{yy} ratio of 0.8.

clearly has an impact on the triggering front as shown in Fig. 4(c). This is supported by the findings of Cuenot *et al.* (2008).

The most interesting finding of our numerical experiments is the influence of the anisotropic initial stress state on the triggering front. Increasing the magnitude of the initial stresses but maintaining the ratio of $S_{h,min}$ to $S_{H,max}$ the aspect ratio of our synthetic microseismicity cloud increases (Fig. 6). One might argue that an anisotropy of the *in situ* stress field of a factor of two is quite extreme, whereas the hydraulic diffusivity may vary by orders of magnitude in different directions, but locally stress concentrations can even lead to higher anisotropies. Our findings indicate that anisotropic initial stresses contribute to the triggering front and would result into potentially different estimates of diffusivity from microseismic observations.

5 CONCLUSIONS

In this paper, we presented a finite-element approach in order to model microseismic event clouds with consideration of an external stress field and including the theory of poroelasticity. This approach introduces several new quantities, which have a major influence on the shape and spatio-temporal evolution of these event clouds. We have shown that there are two possibilities to obtain elongated microseismic clouds: (i) an anisotropic diffusivity as predicted by purely diffusive models by Shapiro *et al.* (2002) and (ii) that the shape of the microseismic clouds are also controlled by the tectonic stress field and oriented along the orientation of maximum horizontal stress. The effect of the far-field tectonic stresses should be considered in the interpretation of the microseismic data recordings. Furthermore, we showed that an implementation of the fluid source with constant injection rate delivers microseismic clouds highly dependent on the rate of injection but less on the hydraulic diffusivity of the rock. However, which implementation of the fluid source is the best remains an open question and needs further quantitative analysis and numerical experiments.

ACKNOWLEDGMENTS

REFERENCES

Altmann, J., Müller, B., Tingay, M., Heidbach, O. & Müller, T., 2008. Towards 3D spatio-temporal pore pressure stress coupling prediction in reservoirs, in *Proceedings of the 70th EAGE Conference,* pp. 4, Rome.

Baisch, S. & Harjes, H.-P., 2003. A model for fluid-injection-induced seismicity at the KTB, Germany, *Geophys. J. Int.,* **152,** 160–170.

Baria, R., Garnish, J., Baumgartner, J., Gérard, A. & Jung, R., 1995. Recent developments in the European HDR research programme at Soultz-sous-Forêts (France), *Ann. Int. Mtg, Int. Geotherm. Assoc., Proc.World Geothermal Congress, Florence, Italy,* 2631–2637.

Barton, N., 2007. *Rock Quality, Seismic Velocity, Attenuation and Anisotropy*, Taylor & Francis, London.

Biot, M.A., 1962. Mechanics of deformation and acoustic propagation in porous media, *J. appl. Phys.,* **33,** 1482–1498.

Bruel D., 2007. Using the migration of induced seismicity as a constraint for fractured Hot Dry Rock reservoir modelling, *Int. J. Rock Mech. Min. Sci.,* **44,** 1106–1117.

Cornet, F.H., Bérard Th. & Bourouis, S., 2007. How close to failure is a granite rock mass at a 5 km depth, *Int. J. Rock Mech. Min. Sci.,* **44,** 47–66.

Cuenot, N., Dorbath, C. & Dorbath, L., 2008. Analysis of the Microseismicity Induced by Fluid Injections at the EGS Site of Soultz-sous-Forets (Alsace, France): implications for the Characterization of the Geothermal Reservoir Properties, *Pure appl. Geophys.,* **165,** 797–828.

Dutta, N.C. & Odé, H., 1979. Attenuation and dispersion of compressional waves in fluid filled porous rocks with partial gas saturation (white-model)—Part I: Biot theory, *Geophysics,* **44,** 1777–1788.

Dyer, B., Juppe, A., Jones, R.H., Thomas, T., Willis-Richards, J. & Jaques, P., 1994. Microseismic results from the European HDR geothermal project at Soultz-sous-Forets, Alsace, France, CSM Associated Ltd., IR03/24.

Engelder, T. & Fischer, M.P., 1994. Influence of poroelastic behavior on the magnitude of minimum horizontalstress, Sh, in overpressured parts of sedimentary basins, *Geology,* **22,** 949–952.

Fehler, M.C., 1989. Stress control of seismicity patterns observed during hydraulic fracturing experiments at the Fenton Hill hot dry rock geothermal energy site, New Mexico. *Int. J. Rock Mech. Min. Sci.,* **26,** 211–219.

Fokker, P.A., 2006. Hydraulic fracturing in the hydrocarbon industry, ENGINE—Enhanced Geothermal Innovative Network for Europe.

Guglielmi, Y., Cappa, F. & Amitrano, D., 2008. High-definition analysis of fluid-induced seismicity related to the mesoscale hydromechanical properties of a fault zone, *Geophys. Res. Lett.,* **35,** L06306, doi:10.1029/2007GL033087.

Hillis, R.R., 2000. Pore pressure/stress coupling and its implications for seismicity, *Explor. Geophys.,* **31,** 448–454.

Hummel, N. & Müller, T.M., 2009. Microseismic signatures related to nonlinear pore-fluid pressure diffusion, *Geophys. J. Int.,* **179,** 1558–1565.

Jaeger, J.C., Cook, N.G.W. & Zimmermann, R.W., 2007. *Fundamentals of Rock Mechanics,* Blackwell Publishing, Malden, MA.

Rothert, E., 2004. Fluid induced microseismicity: data modeling and inversion forhydraulic properties of rocks, *PhD. thesis,* Freie Univ. Berlin.

Rothert, E. & Shapiro, S.A., 2007. Statistics of fracture strength and fluid-induced microseismicity, *J. geophys. Res.,* **102,** B04309, doi:10.1029/2005JB003959.

Rudnicki, J.W., 1986. Fluid Mass sources and point foces in linear elastic diffusive solids, *Mech. Mater.,* **5,** 383–393.

Shapiro, S.A., Audigane, P. & Royer, J.-J., 1999. Large-scale in situ permeability tensor of rocks from induced microseismicity, *Geophys. J. Int.,* **137,** 207–213.

Shapiro, S.A., Rothert, E., Rath, V. & Rindschwentner, J., 2002. Characterization of fluid transport properties of reservoirs using induced microseismicity, *Geophysics,* **67,** 212–220.

Talwani, P., Chen, L. & Gahalaut, K., 2007. Seismogenic permeability, k_s, *J. geophys. Res.,* **112,** B07309, doi:10.1029/2006JB004665.

Wang, H.F., 2000. *Theory of Linear Poroelasticity with Application to Geomechanicsand Hydrogeology*, Princeton University Press, Princeton.

Zoback, M. & Harjes, H.-P., 1997. Injection induced earthquakes and the crustal stress at 9 km depth at the KTB deep drilling site, Germany, *J. geophys. Res.,* **102,** 18 477–18 492.